Monthly Notices
of the
ROYAL ASTRONOMICAL SOCIETY

Mon. Not. R. Astron. Soc. **416,** 715–726 (2011) doi:10.1111/j.1365-2966.2011.19087.x

The expansion proper motions of the planetary nebula NGC 6302 from *Hubble Space Telescope* imaging

C. Szyszka,[1⋆] A. A. Zijlstra[1] and J. R. Walsh[2]

[1]*School of Physics and Astronomy, University of Manchester, Manchester M13 9PL*
[2]*European Southern Observatory, Karl-Schwarzschild Strasse 2, D85748 Garching, Germany*

Accepted 2011 May 16. Received 2011 May 12; in original form 2011 February 24

Downloaded from https://academic.oup.com/mnras/article/416/1/715/1217193 by guest on 24 April 2024

ABSTRACT

Planetary nebulae expand on time-scales of 10^3–10^4 yr. For nearby objects, their expansion can be detected within years to decades. The pattern of expansion probes the internal velocity field and provides clues to the nebula ejection mechanism. In the case of non-symmetric nebulae, and bipolar nebulae in particular, it can also provide information on the development of the morphology. We have measured the expansion proper motions in NGC 6302 from two epochs of *Hubble Space Telescope* (*HST*) imaging, separated by 9.43 yr. This is used to determine the expansion age and the structure of the velocity field. We use *HST* images in the [N II] 6583 Å filter from *HST* Wide Field Planetary Camera 2 and Wide Field Camera 3. The proper motions were obtained for a set of 200 individual tiles within 90 arcsec of the central star. The velocity field shows a characteristic linear increase of velocity with radial distance (a so-called Hubble flow). It agrees well with a previous determination by Meaburn et al., made in a lobe further from the star, which was based on a much longer time-span, but ground-based imaging. The pattern of proper motion vectors is mostly radial and the origin is close to the position of the central star directly detected by Szyszka et al. The results show that the lobes of NGC 6302 were ejected during a brief event 2250 ± 35 yr ago. In the inner regions there is evidence for a subsequent acceleration of the gas by an additional 9.2 km s^{-1}, possibly related to the onset of ionization. The dense and massive molecular torus was ejected over 5000 yr, ending about 2900 yr ago. The lobes were ejected after a short interlude (the 'jet lag') of ∼600 yr during a brief event. The torus and lobes originate from separate mass-loss events with different physical processes. The delay between the cessation of equatorial mass loss and the ejection of the lobes provides an important constraint for explaining the final mass-loss stages of the progenitor stellar system.

Key words: stars: AGB and post-AGB – stars: winds, outflows – planetary nebulae: general – planetary nebulae: individual: NGC 6302.

1 INTRODUCTION

Planetary nebulae (PNe) are among the fastest evolving objects in the Universe. They form when a solar-like star with mass in the range 1–7 $M_\odot$ reaches the asymptotic giant branch (AGB). On the AGB the star develops a degenerate C/O core and a convective envelope which is ejected during a phase of extreme mass loss (e.g. Habing 1996). The ejected envelope expands away from the star with velocities of a few tens of km s^{-1}. The remaining core quickly transitions from a surface temperature of $\sim 3 \times 10^3$ to $\sim 10^5$ K, within $\sim 10^4$ yr, before nuclear burning ceases and the star enters the white dwarf cooling track. The envelope is ionized by the hot core and forms the visible PN.

Since the shell ejection is short lived, expansion of the PN can be observed within decades for nearby PNe. This expansion in the plane of the sky [expansion proper motion (PM)] has been measured for several objects, mostly using Very Large Array and/or *Hubble Space Telescope* (*HST*) observations. By equating the nebula expansion in the plane of the sky with the measured line-of-sight expansion velocity, expansion PMs have been used as a tool for measuring distances (Masson 1986; Hajian, Terzian & Bignell 1993; Meaburn 1997; Palen et al. 2002; Meaburn et al. 2008; Guzmán et al. 2009) and thus stellar masses (Zijlstra, van Hoof & Perley 2008).

The expansion of the PNe is assumed to be spherically symmetric (e.g. Guzmán et al. 2009) or described by a simple velocity law (Zijlstra et al. 2008). But PNe show complex morphologies,

⋆E-mail: cszyszka@gmail.com

© 2011 The Authors
Monthly Notices of the Royal Astronomical Society © 2011 RAS

including tori, bipolar outflows, highly collimated jet-like structures and knots (Balick & Frank 2002). It is unlikely that all these structures expand in spherical unison. In fact, velocity fields and expansion PMs in some cases show evidence of Hubble-like (viz. $V \propto r$) outflows (e.g. Corradi 2004; Meaburn et al. 2008). High-accuracy expansion measurements can reveal the internal dynamics of the complex structures, and thus help to constrain their origin and evolution.

A detailed study of the expansion of the PN NGC 6302 (PN G349.5+01.0) is presented here based on the highest spatial resolution imagery available. NGC 6302 is among the most strongly bipolar (or even multipolar) of the Galactic PN, and has been imaged twice with the *HST*.

Meaburn et al. (2008) measured the PM of 15 features (knots) in the north-western lobe, from two observations separated by a period of 50.88 yr. From the expansion parallax, a distance of 1.17 kpc and an age of 2200 yr were derived. The earlier epoch observation was based on archival photographic plates (Evans 1959). The accuracy is limited by (apart from the time baseline) the image quality of the plate and the seeing of the ground-based observations. To significantly improve on these data, space-based observations are required.

Two sets of *HST* observations taken ∼9.4 yr apart are used in this paper to study the differential expansion of the lobes in the inner regions of the nebula. The *HST* images give a spatial resolution of 0.1 arcsec pixel^{-1}, allowing very compact knots and structures to be resolved, and to thus detect small PMs. Section 2 presents the observations. The reduction and analysis are described in Section 3. The discussion in Section 4 concentrates on the implication of the pattern of the nebula expansion PMs. Conclusions are presented in Section 5.

2 OBSERVATIONS

The PN NGC 6302 has been imaged with the *HST* at two epochs. The first data set was taken on 2000 February 21 (MJD = 51595.93171041) with Wide Field Planetary Camera 2 (WF/PC2). Two narrow-band filters *F*658*N* and *F*656*N* were used for this observation. The second set of imaging observations was made on 2009 July 27 (MJD = 55039.80441102) with Wide Field Camera 3 (WFC3) Ultraviolet and Visible channel (UVIS) as part of the Servicing Mission 4 Early Release Observations. Among the six narrow-band filters used, *F*658*N* and *F*656*N* are in common with the WF/PC2 data. Table 1 presents brief details of both sets of observations.

The existence of two epochs of observation, separated by 3443.8727 d (9.4353 yr), presents the opportunity to directly measure PMs of the expanding nebula. The WFC3 field of view is 162 × 162 arcsec^2. This covers the bright, central region of the nebula. The approximate area covered is shown in Fig. 1, overlaid on a ground-based Hα image covering the full nebula. The older WF/PC2 observations (Matsuura et al. 2005), taken with a smaller field of view, focused on the eastern lobe. The WFC3 data cover most of the nebula, but the expansion could obviously only be studied in the region of overlap. Meaburn et al. (2008) used the opposite, western lobe, and used data at larger distances from the central star than studied here.

Table 1. Summary of *HST* imaging observations of NGC 6302 in 2000 and 2009.

Filter	Date	Integration (s)	Data set
*F*656*N*	2000-02-21	610	U5HH0602B
*F*658*N*	2000-02-21	470	U5HH0602R
*F*656*N*	2009-07-27	2100	IACO01010
*F*658*N*	2009-07-27	2220	IACO01020

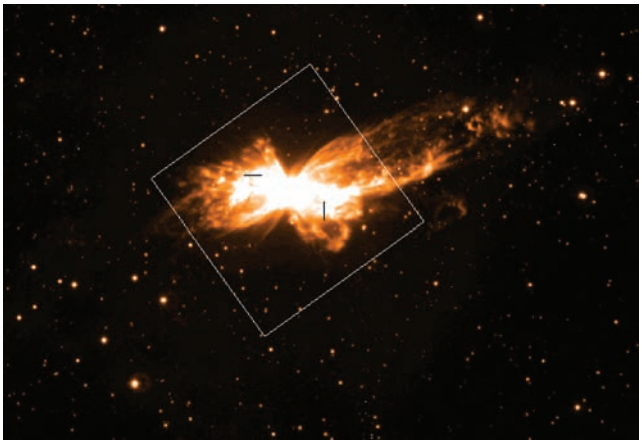

Figure 1. The approximate area covered by the WFC3 images (162 × 162 arcsec^2) is shown by the box, overlaid on a wide-field Hα image of NGC 6302, taken with the Wide Field Imager instrument at the European Southern Observatory 2.2-m telescope. North is up and east is left. The outermost lobes extend over 7 arcmin on the sky.

2.1 Differences in filter transmissions

During both epochs, NGC 6302 was observed with both the *F*658*N* and *F*656*N* filters. Although the filter names stayed the same, the characteristics have changed. The WFC3 filters are narrower, sharper and more efficient than the WF/PC2 filters of the same name, as demonstrated by Fig. 2. The *F*656*N* image is usually called the Hα image, while the *F*658*N* frame is attributed to [N II] emission at wavelength 6583 Å. For the expansion measurements the [N II] image (*F*658*N*) proved to be most suitable and is the one used in this work.

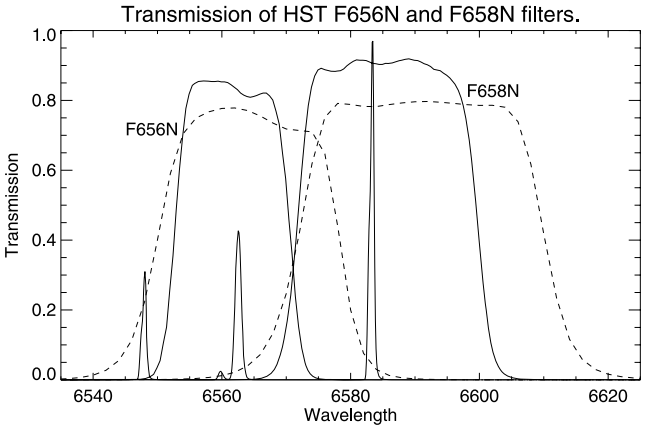

Figure 2. The transmission curves for filters used in *HST* WF//PC2 and WFC3 UVIS cameras. The dashed and the solid lines correspond to WF//PC2 and WFC3 filters, respectively. A reference spectrum of NGC 6302 is also presented, showing the two [N II] lines and the Hα line (flanked by a weak He II line).

Downloaded from https://academic.oup.com/mnras/article/416/1/715/1217193 by guest on 24 April 2024

Table 2. *HST* narrow-band filter transmissions at the wavelengths of the main emission lines.

Instrument	Filter	[N II] 6549 Å	Hα 6565 Å	[N II] 6585 Å
WF/PC2	*F*656*N*	0.22[a]	0.77	0.03
WF/PC2	*F*658*N*	–	0.03	0.78
WFC3	*F*656*N*	0.01[b]	0.81	–
WFC3	*F*658*N*	–	–	0.91

[a]The filter curve is steep at this wavelength. Based on the largest observed velocity shifts on the nebula, the transmission can vary within the range 0.1–0.4.
[b]Similar as for footnote *a*, the transmission ranges from 0.001 to 0.03.

For reference a scaled spectrum of NGC 6302 is shown in Fig. 2 where three brightest emission lines are clearly visible (Hα 6563 Å, [N II] 6548 and 6583 Å). The filter transmissions at these specific wavelengths are listed in Table 2. These filter responses, together with the observed integrated line flux ratios [N II](6549 Å):Hα:[N II](6549 Å) = 1:1.6:3.0 (Tsamis et al. 2003), reveal that about 25 per cent of the total photon count in the WF/PC2 *F*656*N* image comes from the [NII] doublet, while the same ion contributes only about 2 per cent of the total flux for the WFC3 *F*656*N* filter. This makes it more difficult to directly compare these two Hα images. The nebular line wavelengths also depend on the position within the nebula, due to the velocity field (Meaburn & Walsh 1980; Meaburn et al. 2005). This introduces a further transmission uncertainty for the [N II] 6548 Å line which is situated at the edge of the *F*656*N* filter.

The difference in the [N II] contribution causes a notable difference in the two Hα images. The WFC3 image, which isolates Hα much better, shows a smooth emission structure. The WF/PC2 image shows a mixture of this smooth component and a knotty component. This knotty component dominates the *F*658*N* images and is attributed to the [N II] emission. Because of this strong difference between the two Hα images, and the fact that PM measurements are aided by the presence of compact structures, we only make use of the *F*658*N* images here.

A two-colour figure obtained from the WFC3 *F*656*N* and *F*658*N* images is shown in Fig. 3. It shows the complex structure, with the north–south obscuring torus (Matsuura et al. 2005) and the well-defined edges in the lobes.

Figure 3. The WFC3 image, oriented such that north is up and east is left. The *F*658*N* image is blue and the *F*656*N* image is red.

3 REDUCTION AND ANALYSIS

The analysis started with the pipeline-reduced data products, provided by the Hubble Archive hosted by the Space Telescope European Coordinating Facility (ST-ECF). For WF/PC2, data products from version 2.5.1 of the STSDAS calibration pipeline (CALWFP) were used, while for WFC3 UVIS the data were calibrated using version 2.0 of the calibration pipeline (CALWF3). The pipelined images were 'drizzled' (i.e. created by combining images with subpixel shifts) using the task 'multidrizzle' in STSDAS. This also corrects for the geometric distortion of the respective cameras.

Further reductions to improve the astrometric calibration and the geometric distortions were applied and are detailed below.

3.1 Astrometry calibration

The absolute astrometry as returned by the pipeline reduction is based on Guide Stars Catalogue (GSC2), which have a typical positional uncertainty of 0.2–0.28 arcsec depending on magnitude (Lasker et al. 2008). Depending on the sets of guide stars used, the astrometry for both sets of observations can differ. In addition, the WFC3 data had not been fully calibrated at the time the observations were reduced, so larger errors may be present in the pipeline calibration.

To improve the relative astrometry of the two sets of images, we identified common field stars present in both epochs. The stars were identified from the Two Micron All Sky Survey (2MASS) catalogue (Skrutskie et al. 2006), being the most complete stellar catalogue at the relevant magnitude levels. Catalogue stars were excluded where two sources were visible in the *HST* images within a circle of 1-arcsec radius from the 2MASS position (which would be merged at the 2MASS resolution). Stars were also excluded if they were farther than 1 arcsec from the 2MASS position, taken as evidence for large PM.

For the WF/PC2 frame, the astrometric solution was tested using the astrometry tool in GAIA/Starlink with the 2MASS catalogue in the field of view (rejecting galaxies). The solution showed an individual scatter in the stellar positions of around 0.3 arcsec and a mean shift of 0.1 arcsec ($\approx$1 pixel). The procedure was repeated with the WFC3 image. This latter step revealed a distinct $\sim$3 arcsec shift (about 75 WFC3 pixels), attributed to the pipeline reduction of these early in-flight data. This shift was corrected within GAIA by a translation in RA and Dec., assuming no rotation and a constant pixel scale.

At this point, the WFC3 and WFC2 images have the same astrometry but different pixel scale and orientation. We rotated the images to a north-east orientation (for the WF/PC2 image this was already done by the pipeline), and rebinned the higher resolution WFC3 data (0.04 arcsec pixel^{-1}) to the resolution of WF/PC2 chips (i.e. 0.1 arcsec pixel^{-1}), bringing both frames on to the same spatial grids. This was done utilizing the MONTAGE software tool.

In a third step, for the 2MASS stars in common between both epochs, the centroid positions were measured in GAIA/Starlink in each frame to test for shifts. Sources which presented a shift between the two epochs larger than 1.4 pixel (0.14 arcsec) were excluded, suspected to be stars with high PM (this step removed five stars). This left 54 stars in common between both frames. The histogram of the shifts between these 54 stars is shown in Fig. 4 (the shaded area). This distribution is rather wide, suggesting a possible residual astrometric error.

Comparing the difference in the positions of the stars on the WFC3 and WF/PC2 images as a function of *x* and *y* pixel number

Downloaded from https://academic.oup.com/mnras/article/416/1/715/1217193 by guest on 24 April 2024

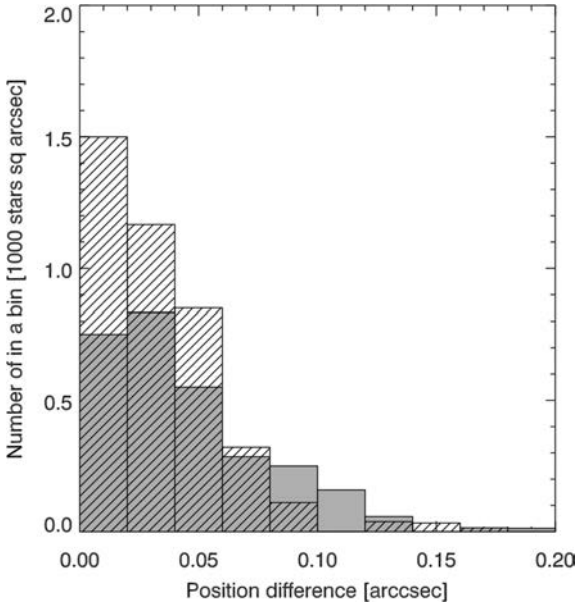

Figure 4. Histogram of the measured stellar position differences between WF/PC2 and WFC3 UVIS images. The hatched region shows the histogram of the position differences before correction for shear (see Fig. 5), and the shaded region after correction for shear. A difference of 0.1 arcsec is equal to 1 pixel.

shows that there is indeed a residual distortion in one (or both) of the images, with an amplitude of about 0.1 arcsec from edge to edge. The shear between both sets of images is clearly visible in Fig. 5. We fitted the difference in star position versus pixel number, separately for x and y, with a linear function of pixel number ($x' - x = a_1x + b_1$ and $y' - y = a_2y + b_2$), where the primed coordinates are the corrected ones. The best fit yielded (a_1, b_1)=(0.0006378, −0.0727) and (a_2, b_2)=(0.0007481, −0.2905). The reliability of this transformation is limited by the intrinsic PM of the stars which is not known. The constants a_1, a_2 indicate a small difference in pixel scale, which needs to be corrected: the fact that both axes yield the same factor within the uncertainties gives us confidence that this is valid. The constants b_1, b_2 show a misalignment between the frames, largest in y. We applied the a and b coefficients to the WFC3 image.

This correction improved the astrometric calibration, as demonstrated by the hatched histogram in Fig. 4. The mean scatter in stellar positions is now better than 0.05 arcsec (Fig. 6). This is probably dominated by the PMs of the individual stars. The motion corresponds to about 25 km s^{-1} at a distance of 1 kpc which is of the order of the expected stellar velocity dispersion in the Galactic plane. The accuracy of the relative alignment between the two images, as measured from the error on the mean, is approximately 0.01 arcsec.

3.2 Proper motion measurements

3.2.1 Expected shifts

The expected level of PMs can be estimated from the existing measurements of Meaburn et al. (2008). They detected PMs in the north-western lobe (see Fig. 1), between 1 and 3 arcmin from the centre of the nebula. Their innermost measurement derives from a feature at 1.06 arcmin from the centre of the nebula, and revealed a

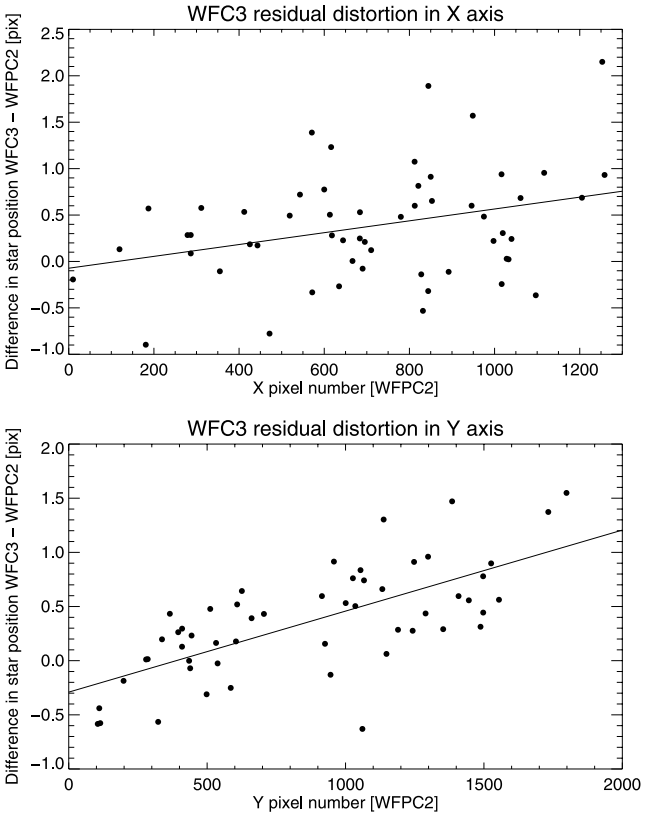

Figure 5. Distortion of the WFC3 UVIS relative to the WF/PC2 as revealed by comparison of the positions of stars in common on both images.

PM of 29.5 mas yr^{-1}. At large distances, they find a linear increase of PM with distance.

The most distant features measured in this work extend up to about 1 arcmin from the centre of the nebula, matching well with the innermost measurement of Meaburn et al. (2008) (albeit at opposite side of the nebula). The two epochs of *HST* imaging are separated by ≈10 yr. Thus, we expect shifts up to 0.3 arcsec in the outer area

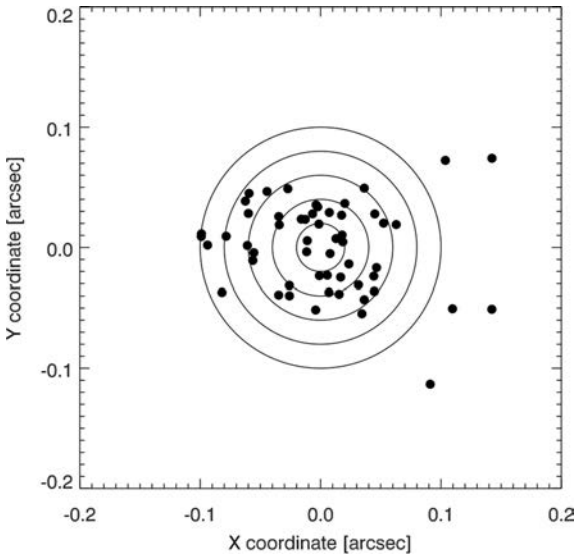

Figure 6. Measured difference of the positions of individual stars between the two epochs, after correction for shear. The concentric circles correspond to the inner five bins of the histogram of Fig. 4.

Downloaded from https://academic.oup.com/mnras/article/416/1/715/1217193 by guest on 24 April 2024

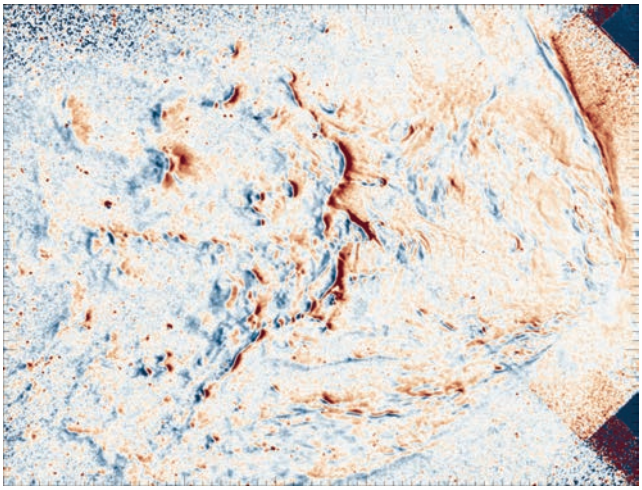

Figure 7. The difference image between the WF/PC2 and WFC3 *F*658*N* images, oriented such that north is up and east is left. The CCD layout of the WF/PC2 is visible, with the smaller PC image on the right. Blue shows excess emission in WFC3, and red in WF/PC2. The shifts increase towards the left, further from the centre.

of the *HST* images, down to 0.1 arcsec at 20 arcsec from the centre. The latter corresponds to 1 pixel, and is 10 times larger than the alignment errors derived in the previous section.

3.2.2 Method

Direct evidence for PM of the structures in the nebula can be seen from difference imaging. This is shown in Fig. 7. The pattern shows clear motion of sharp-edged features, in most cases directed away from the centre of the nebula. In the display, we used the arctan of the differential intensity, to flatten the image. In reality, the amplitudes in the right part, close to the centre, are much higher than on the left. The strong effect seen on the northern edge of the obscuring torus (top right) is not caused by a very large motion, but represents a braided structure with one chain brightening and the other fading. The intensity changes may be partly caused by the Hα emission in this region, which affects the two filters differently. The results below indicate that the gas flow in this region is along the linear feature.

The PM cannot be directly measured from the difference image. In regions where there is a field star close to a nebular feature, the motion can be measured with respect to the reference star. In areas without such a reference point a more detailed comparison is required. The accuracy of the PM is limited by the fact that the nebular features are not point sources, but are extended. This introduces uncertainties which are much larger than the systemic error derived from stellar (point) sources.

The best measurement for the PM is obtained by shifting the two images and calculating the χ^2 of the difference image. This technique works for extended emission features, as long as the region studied is sufficiently small that a linear shift provides a good approximation, whilst there is sufficient structure in the emission features within this region. We implemented this technique by considering the nebula as an array of adjoining square tiles. To ensure sufficient structure within the selected region, we chose to cut the nebula into a 23×19 grid of fairly large square tiles, 41×41 pixels in size (4.1×4.1 arcsec^2; 437 tiles in total.)

To determine the shift for each tile, we employed the MPFIT IDL package (Markwardt 2009). This finds the best matching model iteratively by means of χ^2 minimization, with as parameters the shift in x and y (PM of the nebular features) and the scaling factor for the intensity. The scaling factor for the intensity accounts for the sensitivity difference between WF/PC2 and WFC3. For each step (each shift) in this procedure, the WFC3 image was interpolated to the pixel frame WF/PC2 image, before the χ^2 of the difference image was calculated. This interpolation required non-integer shifts, and was done using the IDL function INTERPOLATE.

The interpolation of the WFC3 image was always done using the entire WFC3 image. This avoids edge effects on the extracted squares. The difference image was obtained for the analysed tile only.

3.2.3 Uncertainties

To assess the intrinsic errors of this method, we artificially introduced a shift to the WF/PC2 image, and next used the same method on the original and shifted WF/PC2 images. The aim was to reproduce the shift. This measures both the intrinsic uncertainty in the calculation and the reliability of each tile.

We used shifts of $(-2.0, -1.0, -0.8, -0.3)$ pixels in both directions, extracted the full set of tiles, and reran the analysis for each tile. For integer pixel shifts, the introduced shift was reproduced with accuracy close to the computational precision for single-precision numbers, with standard deviation of 10^{-5} pixel. (The standard deviation excludes tiles where the calculated shift differed from the applied shift by more than 10 per cent.)

Not all tiles produce consistent results. Large errors are found for tiles which lack nebular emission structure necessary for an accurate determination of the shift. We exclude tiles where the calculated shift was in error by more than 50 per cent for all of the trial shifts. This removed all tiles without detected emission in the WF/PC2 image (the WFC3 image is deeper and shows emission in some tiles which are empty in WF/PC2). It also removed a few tiles in regions with smooth emission. It left 246 tiles.

Subsequently, we ran the full analysis on the WFC3 versus WF/PC2 image, extracting the determined shifts for the tiles identified in the previous step. A number of tiles were affected by field stars, which may move differently from the nebula. These tiles (a total of 46) were manually removed. We also removed tiles with very large shifts or where the shift measurements in one of the two axes had failed. The final sample of 'good' tiles for PM measurements is 200.

The MPFIT routine returns the measured shift, separately for x and y, and the error on these shifts determined from the χ^2 minimization. Fig. 8 shows the reported 1σ uncertainties as function of the factual measurements for both axes. The formal errors yield a typical signal-to-noise ratio (S/N) in excess of 100 for our observed shifts. Significant clustering is visible in the x-axis shifts, around the integer values. The measured values avoid the range between $(-1.0, -1.1)$ and $(-2.0, -2.2)$. There may also be an excess at 0. This appears to be a numerical artefact of the interpolation procedure, which is part of the core IDL package. This artefact must be taken into account during interpretation.

In the large majority of tiles, the uncertainty is less than 0.01 pixel, or 1 mas. The artefact discussed above amounts to errors of order 0.1 pixel, which over a 10 yr time-span is still only 1 mas yr^{-1}. This is likely to be the best achievable as the test was done under 'ideal' circumstances of no change in emission apart from the motion. The real uncertainty is harder to quantify. However, the spread in observed PMs for different tiles, as shown in Fig. 10, provides an

Downloaded from https://academic.oup.com/mnras/article/416/1/715/1217193 by guest on 24 April 2024

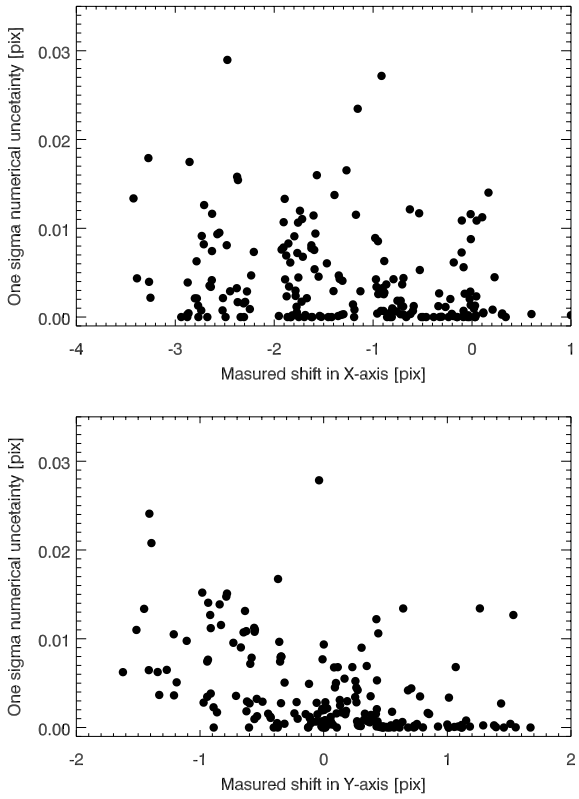

Figure 8. Formal numerical uncertainties, as derived by MPFIT procedure, plotted versus measured shift for *x*- (top) and *y*-axes (bottom).

indication for this. The spread amounts to an rms of 5 mas yr^{-1}, five times worse than that derived from the numerical uncertainty. The spread does not seem to increase with distance from the centre, where the emission is fainter by two orders of magnitude. This indicates that we are not limited by S/N on the emission, but by the presence of nebular structures needed to detect PM.

3.2.4 Results

Fig. 9 shows the PM velocity field. The boxes show the squares which were classified as 'good' by the automatic fitting routine on the test shifts. The arrows show the measured PM. If the box is empty, that specific measurement was flagged as 'bad' manually, either because of the presence of a field star or because of lack of nebular structure. The yellow arrows indicate measurements where one of the axes returned a zero error; this may in cases be related to the numerical artefact listed above. The confidence in the direction of these vectors is reduced. All remaining vectors have good confidence. The length of each arrow is proportional to the PM. The bar at the bottom right shows a PM of 20 mas yr^{-1} (0.2 pixel over 10 yr). The magenta symbol at the centre of the nebula shows the position of the central star from Szyszka et al. (2009).

A very regular velocity field emerges, largely radial from the location of the central star (Szyszka et al. 2009), at all distances from the star. The vectors are well aligned with the nebular structures, in particular the bright linear structures delineating the obscuring torus where the flow is along the structures. The shock-like structure embedded in the centre of the eastern lobe [from tile (37 arcsec, 15 arcsec) to tile (45 arcsec, −14 arcsec)] moves radially, at an angle to the front; however, where such a structure develops a tail [e.g. tile (55 arcsec, 18 arcsec)], the tail is along the flow direction. Such tails are seen especially in the outer regions, and appear to be a flow-driven phenomenon.

4 DISCUSSION

4.1 Hubble flow

So-called Hubble-like outflows (viz. recession velocity $\propto$ distance) have been found in a number of bipolar PNe (Corradi 2004; Jones et al. 2010) and appear to be relatively common in such objects. In the case of NGC 6302, such a velocity law was first reported by Peretto et al. (2007), as a component in molecular CO lines close to the expanding torus: their fig. 10 shows a clear linear dependence of velocity with distance. A Hubble flow in the lobes was reported by Meaburn et al. (2008), based on a tight correlation between PM of 15 individual knots and distance to the central star. In 'normal' (non-bipolar) nebulae, the expansion velocity increases outwards because of the overpressure of the ionized region (e.g. Gesicki, Acker & Zijlstra 2003). However, the linearly increasing Hubble flows are more likely related to short-lived ejection events (Huggins 2007) or fast changes in outflow velocity (Zijlstra et al. 2001).

In Fig. 10, the dependence of the PM magnitude versus separation of the individual knot from the central source is plotted for our *HST* data (including all measurements presented in Fig. 9). We assume that the central star is the point source revealed by the imaging in the WFC3 *F*683*N* filter, at the position $\alpha = 17^{\rm h}13^{\rm m}44\overset{\rm s}{.}39$, $\delta = -37^\circ06'12\overset{''}{.}93$ (Szyszka et al. 2009). The data points from Meaburn et al. (2008) are presented in this figure by open circles. We find that a linear relation provides an accurate representation of the results. The measurements of Meaburn et al. fall on the same line, in spite of being located on the opposite side of the nebula, and in most cases at much larger distances from the star. The *HST* points extend to 70 arcsec from the star, while the Meaburn knots range from 60 to 180 arcsec. Thus, both lobes have a common origin.

A linear fit is shown in Fig. 10. The parameters of this best fit, obtained from combining the *HST* and Meaburn et al. data (214 data points), are given by

$$y = ax + b = 0.445x + 0.58, (\sigma_a = 0.01, \sigma_b = 0.51), \quad (1)$$

where y is the PM in mas yr^{-1} and x is the distance to the centre in arcsec. We quantified the spread of points about the fitted line by calculation of the standard deviation, which was $\sigma = 4.04$. This quantity is indicated in Fig. 10 by parallel dotted lines.

Fig. 10 shows a number of points falling somewhat below the fitted line. Fig. 9 shows the location of these vectors, encoded by the green boxes. Most of these vectors come from tiles with relatively smooth emission, or from tiles only containing linear features along the flow direction; all are low-confidence points marked by yellow arrows. We conclude that 'green' points can be safely omitted from the fit. Refitting the line excluding these lower points (186 points) yields

$$y = ax + b = 0.446x + 1.67, (\sigma_a = 0.007, \sigma_b = 0.32). \quad (2)$$

The blue vectors show the points more than 1σ above the fit. These are predominantly found in the lower right corner. Excluding also the higher points we retain 165 data points which result in fit

$$y = ax + b = 0.444x + 1.12, (\sigma_a = 0.006, \sigma_b = 0.31). \quad (3)$$

The fit remains the same within the errors, but the spread is significantly reduced. Without the lower points, the spread is 2.9 mas yr^{-1}, which is a reasonable value for the measurement error on good squares.

Downloaded from https://academic.oup.com/mnras/article/416/1/715/1217193 by guest on 24 April 2024

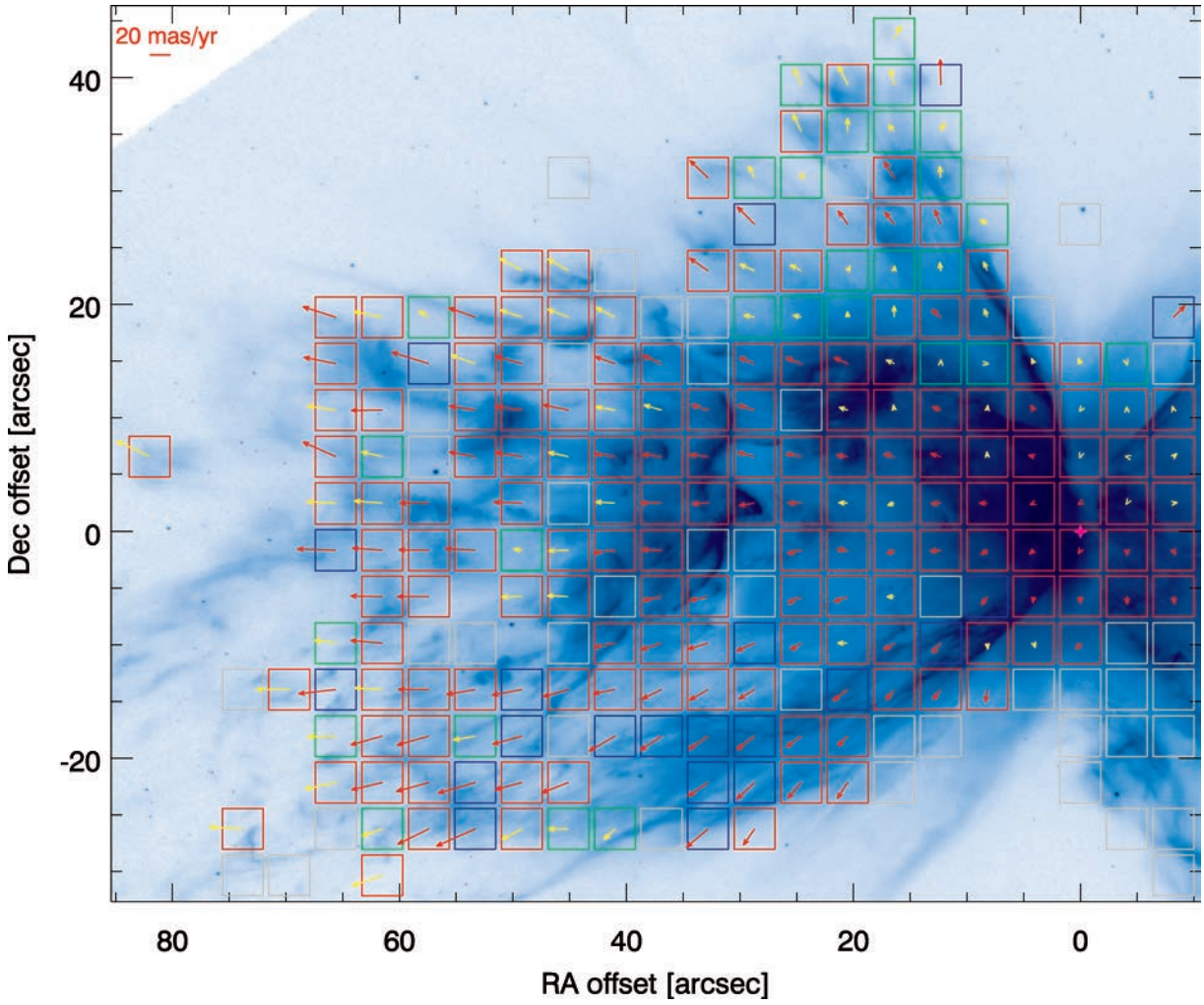

Figure 9. The PM velocity field of NGC 6302, derived from the two *HST* images 9.44 yr apart. The blue image is the 2009 WFC [N II] image. Arrows indicate the measured PM for each 4.1 × 4.1 arcsec^2 tile. Yellow arrows indicate measurements where one of the axes is in doubt. Red arrows give the most accurate results. The length of each arrow indicates the PM; the bar at top left corresponds to a value of 20 mas yr^{-1}. The typical uncertainty is estimated at 5 mas yr^{-1}. For empty boxes, the measurement was classified as 'bad' and dropped. Colouring of boxes corresponds to quality of the fit to the Hubble flow relation (see Fig. 10), with red points falling within 1σ, blue at least 1σ above the fitted relation and green at least 1σ below the PM-separation relation. The reference position (RA offset, Dec. offset) = (0, 0) is the position of the central star RA=$17^{\rm h}13^{\rm m}44\overset{\rm s}{.}39$, Dec. = $-37^\circ06'12\overset{''}{.}93$(J = 2000) (Szyszka et al. 2009).

As the *HST* and Meaburn data are well fitted by a single line, we conclude that the Hubble flow detected by Meaburn et al. (2008) extends to the innermost parts of the nebula.

Meaburn et al. (2005) find that the outer lobe is tilted with respect to the plane of the sky at an angle of 12.8° (77° to the line of sight). The current data do not restrict the angle of inclination for the inner lobe, as the measured PM versus distance is inclination-independent. In published archival spectra (Meaburn & Walsh 1980; Meaburn et al. 2005), an additional radial-velocity component is clearly visible in the inner regions attesting to the presence of multiple components that may not occupy the same range of inclination angles. Thus, it is likely that a broader range of inclination angles exists in the inner flow.

The Hubble-like flow reported by Peretto et al. (2007) in molecular CO lines is detected in radial velocity, within the inner 20 arcsec. The increase of the radial velocity is ≈24 km s^{-1} over 15 arcsec, or 280 km s^{-1} pc^{-1}, in the blueshifted component. The Hubble flow reported in this work gives a tangential velocity gradient of 410 km s^{-1} pc^{-1}. If these components trace the same outflow, the inclination to the line of sight is 56°. The redshifted CO component shows a minor Hubble flow with a similar gradient, indicating a similar inclination to the line of sight. This symmetry is consistent with Meaburn et al. (2005) finding that the lobes are oriented close to the plane of sky.

The velocity gradient of the Hubble flow derived from the tangential velocity, 410 km s^{-1} pc^{-1}, gives the correct value, as both velocity and distance are projected by the same factor.

4.2 Age of the nebula

Meaburn et al. (2008) reported an age of ≈2200 yr. The global age of the nebula can be derived from the slope of the Hubble flow relation. In this work it varies between 0.44 and 0.45 mas yr^{-1} arcsec^{-1} (see equations 1–3), which translates to an age of 2250 ± 35 yr.

The large number of individual measurements allows us to study the age of the nebula in more detail. The separation of specific fragments of the nebula from the central star divided by their measured PM gives the dynamic age of this patch of the nebula. The

© 2011 The Authors, MNRAS **416,** 715–726
Monthly Notices of the Royal Astronomical Society © 2011 RAS

Downloaded from https://academic.oup.com/mnras/article/416/1/715/1217193 by guest on 24 April 2024

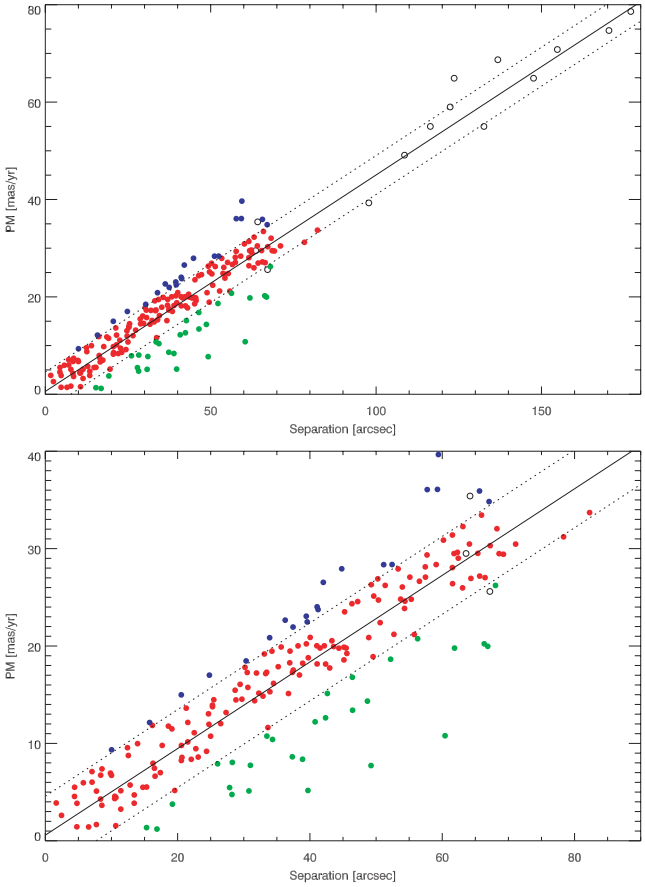

Figure 10. The PMs derived for 200 individual tiles are plotted versus separation from the central source. Filled circles represent this work, open circles from Meaburn et al. (2008). Note that Meaburn's measurements are from the north-western lobe of the nebula, while this work concentrates mainly on the east lobe. The diagonal line represents the best fit to all data (see equation 1) with an indication of $\pm 1\sigma$ dotted lines. Colouring of the points distinguish measurements falling within $\pm 1\sigma$ form the fitted relation (red points), from the measurements falling at least 1σ above or at least 1σ below fitted relation (blue and green points, respectively). This colouring convention will be used in all subsequent figures.

distribution of these ages as function of distance from the star is plotted in Fig. 11. If all the nebular structures were ejected at the same time, and the velocity field remained unchanged since the ejection, the distribution in Fig. 11 would be flat. This is not the case for NGC 6302. The scatter increases towards the central star because of the large effect of measurement errors. However, allowing for this, there is a clear indication that the inner parts of the nebula appear dynamically younger than the outer parts.

To explain this phenomena, let us make the assumption that the nebula experienced an additional act of acceleration at some point during its evolution. If this occurred very recently (compared to the time of ejection of the AGB envelope), it will alter the nebular velocity field but not yet the position of each specific fragment of the nebula. This will reduce the apparent ages; the reduction will be largest in the inner part of the nebula where the pre-acceleration velocities were the smallest.

We model this by adding an extra velocity component

$$v = v_0 + v_c. \tag{4}$$

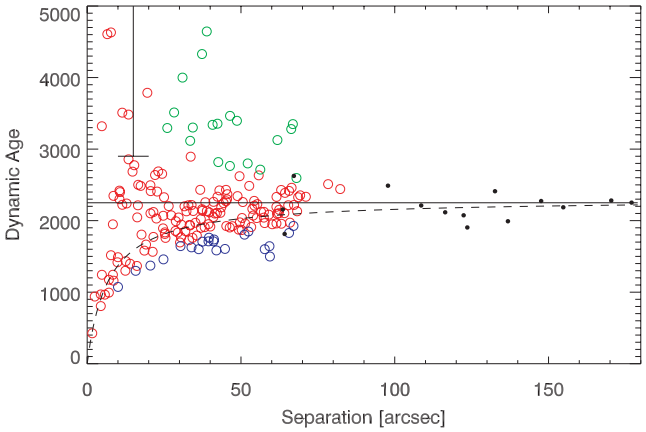

Figure 11. The ages of individual knots are plotted as a function of distance from the central star. Models discussed in text (equation 5) are presented with lines. The solid line uses parameters from the fit to all measurements (see equation 1), while the dashed line represents a fit without excluded low-confidence points (see equation 2). The vertical bar indicates the mass-loss phase with cessation at 2900 yr (Peretto et al. 2007). The colour of the points is as in Fig. 9.

The modified age t' (yr) can be described by the formula

$$t' = \frac{10^3 r}{v_0 + v_c} = \frac{t_0}{1 + v_c t_0 / 10^3 r}, \tag{5}$$

where r (arcsec) is the separation from the central star, v_0 (mas yr^{-1}) the initial velocity and v_c (mas yr^{-1}) represents the additional velocity component. The conversion factor 10^3 (mas arcsec^{-1}) is needed for conservation of units. For small v_c, the modified age t' becomes t_0 and is a constant function of separation. Equation (5) can be also presented as a function

$$v(r) = \frac{10^3}{t_0} r + v_c, \tag{6}$$

which has the same form as the linear fit to the PM data in Fig. 10. Thus, the fitted parameters in equations (1)–(3) represent $a = 10^3/t_0 (1\,\mathrm{yr}^{-1})$ and $b = v_c\,(\mathrm{mas\,yr}^{-1})$.

The solid line in Fig. 11 shows this model for the fitted parameters of equation (1). Excluding the low-confidence points above the relation (the green points), as fitted in equation (2), gives the dashed line. The dashed line gives a derived age t_0 of the nebula slightly less than before, of 2240 yr.

The best fit reveals an acceleration that occurred in the PN phase and resulted in a velocity increase of $v_c = 9.2\,\mathrm{km\,s}^{-1}$. A similar effect was observed in Gesicki et al. (2003) where extra acceleration was needed at the inner edge of a nebula to explain the velocity broadening of profiles of high-excitation ions.

The same kind of internal acceleration was reported by Peretto et al. (2007) in their fig. 10. The Hubble flow derived from radial velocity CO observations at the offset 0 (arcsec) does not have a zero velocity. Instead, the slope of Hubble flow relation starts at a velocity of $V = V_{\mathrm{LSR}} + 12\,\mathrm{km\,s}^{-1}$.

4.3 Nebula asymmetries

The consistency of the Hubble flow throughout the lobes indicates that the expansion is homologous, and effectively free-flow. As derived in Section 4.2, there is some evidence for additional acceleration; although this affects the inner regions most, it may in fact be present throughout the nebula.

Downloaded from https://academic.oup.com/mnras/article/416/1/715/1217193 by guest on 24 April 2024

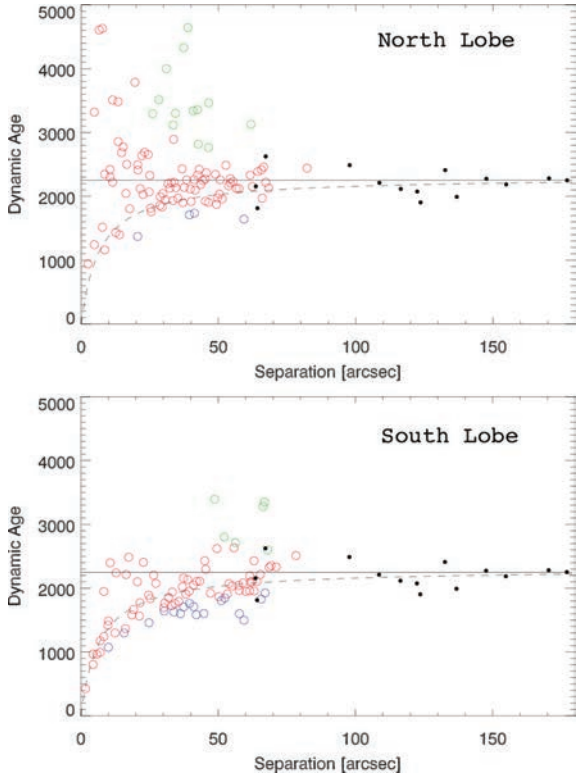

Figure 12. The same as Fig. 11, but northern tiles (Dec. offset ≥0 in Fig. 9) are plotted in upper panel and southern tiles of the nebula are plotted in lower panel. The apparent age distribution differs in the northern and southern parts of the nebula. The effect is attributed to additional acceleration present in the southern lobe. The dashed line represents the modified age t' with parameters from equation (7). The fit to the southern tiles was made in PM-separation space and is presented in Fig. 13. The solid horizontal line indicates an age of 2250 yr. The colouring of the points is as in Fig. 10.

However, there appear to be some differences in kinematics between different regions. The tiles where the gas is moving faster than expected (the blue points in Fig. 10) are primarily located in the southern part of the nebula (the blue-edged tiles in Fig. 9).

To show this, we divided the tiles into two samples, depending on the offset in Fig. 9. The northern tiles are defined as those where the declination offset ≥0 arcsec relative to the position of the central star and the southern tiles are those with offset ≥0 arcsec. The apparent age (t') distribution for both samples is presented in Fig. 12. Very few tiles from the southern part of the nebula appear to be older than 2250 yr, compared to the northern tiles. The effect of the additional velocity component is also much clearer in the southern part of the lobe. The differences are seen mainly within 50 arcsec of the central star.

We fitted the Hubble flow relation to the southern subsample of the nebula. We excluded points falling outside the $1\sigma = 4.04$ (mas yr^{-1}) upper and lower threshold of the distribution, in the same way it was done for equation (1)–(3). The refitted relation is

$$y = ax + b = 0.429x + 2.71, (\sigma_a = 0.011, \sigma_b = 0.7). \quad (7)$$

The fit is presented in Fig. 13. The parameter $b = v_c = 2.71$ (mas yr^{-1}), expressed as the velocity in the plane of the sky, equals $v_c = 15$ km s^{-1}. This is a bit higher than previously found for the whole nebula.

The nature of these velocity asymmetries is not well understood. In Fig. 9 we note a cluster of short vectors predominantly along the northern edge of the eastern lobe. These represent the measurements

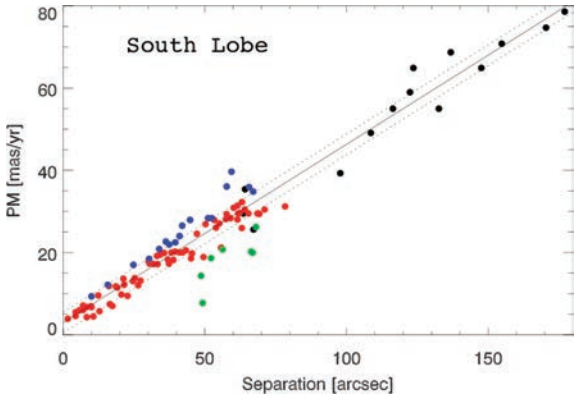

Figure 13. The same as Fig. 10, but only southern tiles (Dec. offset ≥0 in Fig. 9) are plotted. The fit (solid line) is made to those measurements excluding outlaying points (see equation 7), 1σ uncertainties are indicated with the dotted lines above and below. The colouring of the points is as in Fig. 10.

with large dynamical ages (≥2700 yr). In the southern section of the nebula we observe higher velocities, thus younger dynamical ages, at the same distance from the star. This cannot be due to a difference in inclination with the line of sight, as this projection effect disappears in the Hubble diagram. One possibility is that the northern region has undergone deceleration; another possibility is that the innermost southern region is younger. A plausible model for the development of multipolar nebulae is the warped disc model of Icke (2003), suggested to be applicable to NGC 6302 by Matsuura et al. (2005). In this model, the most elongated lobes develop only once the stellar wind breaks through the constraining disc. This happens after a significant time delay. It is noteworthy that the southern, younger vectors in NGC 6302 are found point symmetrically to the most elongated north-western lobe (Meaburn et al. 2005).

4.4 Centroid of PM measurements

With a sufficient number of PM vectors we can attempt to find the point of common origin of these velocities. Two methods were used to test whether the PM vectors converge in one point. The first is a propagation of each measurement back in time, conserving its direction. The time is derived from the distance to the assumed central position. Each vector gives a position at the same distance as assumed for the central star position. The second is a more novel technique called *criss-cross mapping* (Steffen & Koning 2011), and relies solely on directions of vectors.

In the first approach we propagated the PM vector in the opposite direction to the measured motion. We assumed that the age t' (yr) for each specific fragment of the nebula at the distance r (arcsec) can be described by equation (5) using parameters from the fit to the Hubble flow relation (see equation 2). The derived age together with the PM vector defines the 'origin' point of this specific part of the nebula. The result is presented in Fig. 14, with the same colouring conversion as in Fig. 10. The background is the optical image of the nebula. We can see that the convergence is rather poor. Out of 200 considered PM measurements, 155 fall within the circle of 10 arcsec from the central star. These are mostly (133) 'red' points which follow the Hubble flow relation reasonably well (see Fig. 10). We also find 11 'blue' origin points above this relation; notably, none of the 'green' points was found within the 10-arcsec circle.

Downloaded from https://academic.oup.com/mnras/article/416/1/715/1217193 by guest on 24 April 2024

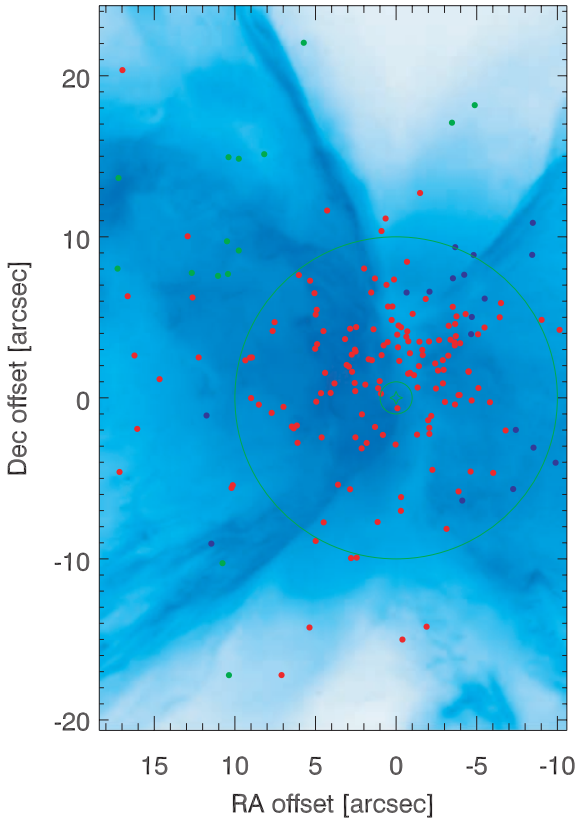

Figure 14. The origins of the PM vectors are plotted against inner parts of the NGC 6302 (blue image). For each fragment of the nebula at the distance r, we adopted age t' according to equation (5), and fitted values from equation (2) $v_c = 1.67$ (mas yr^{-1}) and age $t_0 = 2220$ (yr). The position of the central star is indicated by the green star. The 1 and 10 arcsec circles are plotted for the reference. The (0,0) point corresponds to the position of the central star. North is up, east is left.

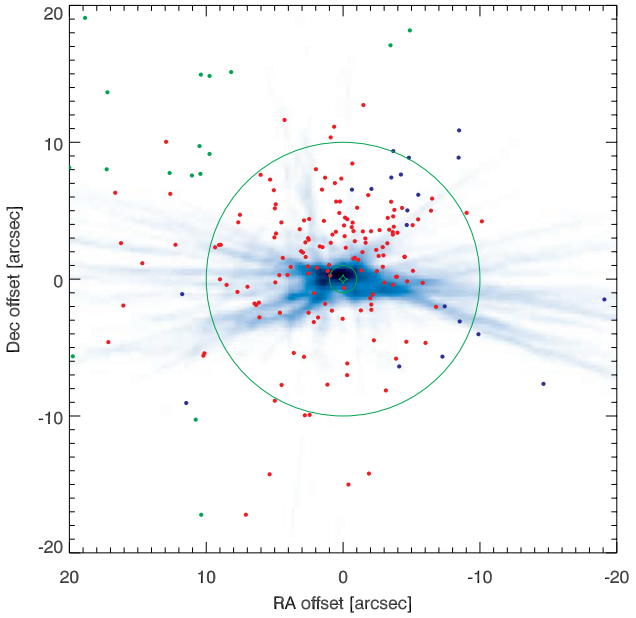

Figure 15. The criss-cross mapping of the PM vectors (the blue image) compared to the origins of the PM vectors calculated as discussed in text and Fig. 14. The blue background is the criss-cross map constructed from measured PM vectors. The colouring of the points is as in Fig. 10. The 10-arcsec circle is plotted for the reference. The (0,0) point corresponds to the position of the central star. North is up, east is left.

The criss-cross mapping is implemented in the modelling tool Shape (Steffen et al. 2010). In this technique we construct a map of crossing points between all the measurements, much like an intensity map. Each PM vector is represented as an infinite line, with some width. At the crossing point the number of lines is added up. The peak of the number density map indicates the position where the largest number of PM vectors crossed each other.

The result of criss-cross calculation is presented in Fig. 15. The number density map is squared to highlight regions with the highest probability to be a centroid of the PM velocity field. The origin points from the previous method are overplotted for reference. The convergence is very close to the central star position [the (0,0) offset on the map], with an offset of only ≈0.5 arcsec north. The criss-cross analysis provides support for the identification of the point source found by Szyszka et al. (2009) as a central star. The fact that most of PM vectors cross the position of the central star indicates that the velocity field is mostly radial.

The two methods show different results. The fact that for the first method the PM vectors do not converge to a common origin point is attributed to the variations in velocities due to the kinematic effects discussed above. The second method showed that a large number of the PM vectors indeed cross at the position of the central star. If we apply this result in the first method, we conclude that the age was underestimated (for the northern lobe) or overestimated (for the southern lobe).

4.5 The molecular torus and ionized centre

The nebula has a prominent high-extinction torus (Matsuura et al. 2005). This torus is also detected in CO, is oriented north–south, extends from 5.5 to 12 arcsec (Peretto et al. 2007), and has an estimated dust mass of $M_{\rm dust} \sim 0.03 M_\odot$ and a total mass of $M_{\rm gas} \approx 1 M_\odot$ (Matsuura et al. 2005). [Peretto et al. (2007) improved the torus mass estimation to $\approx 2 M_\odot \pm 1 M_\odot$. Dinh-V-Trung et al. (2008) however derive a much lower mass of $0.1 M_\odot$, based on almost identical data. This value is surprisingly low given the extremely high extinction (Matsuura et al. 2005), but it shows that the mass determinations remain uncertain.]

The molecular torus reported by Peretto et al. (2007) is centred at declination $\delta = -37^\circ 06' 12\farcs5$. The declination of the central star is $\delta = -37^\circ 06' 12\farcs93$, whilst the peak of the criss-cross map is about 0.5 arcsec north at $\delta = -37^\circ 06' 12\farcs5$. All these positions agree to within the uncertainties. The torus has an age of 2900 yr, based on its size and the expansion velocity of 8 km s^{-1} (Peretto et al. 2007).

The region inside of the molecular torus is not devoid of gas. There is an inner, ionized torus, located within the central few arcseconds (Gomez et al. 1989). This ionized torus is also expanding (Gomez, Rodriguez & Moran 1993), at a fractional growth rate of 8.36×10^{-4} yr^{-1}, which gives a dynamic age of 1200 yr, making it much younger than any other part of the nebula. There are uncertainties in this measurement. The ionization front travels faster than the gas by as much as 40 per cent and this can lead to overestimation of measured expansion rates of ionization-bounded nebulae, as found for the case of NGC 7027 by Zijlstra et al. (2008). [Gomez et al. (1993) apply their expansion to the inner radius, assuming a Hubble-type velocity field but this retains the uncertainty.] A second problem is that the velocity field in the ionized region can be altered by the overpressure caused by the ionization, leading to acceleration. The nature and evolution of the inner torus is not yet fully understood. The expansion of the inner torus appears to be

Downloaded from https://academic.oup.com/mnras/article/416/1/715/1217193 by guest on 24 April 2024

in the same direction as the faster (younger) PM vectors measured by *HST* in the south-eastern part of the nebula, and there may be a relation between these two regions.

The *HST* data do not allow us to study the expansion of the inner 4 arcsec of the nebula as this is approximately the size of the single tile which is 4.1×4.1 arcsec^2. Because of the lack of clear features in this highly obscured region, we have also been unable to make an expansion map of the inner regions at higher spatial resolution.

4.6 Mass-loss history of NGC 6302

We find three separate components in NGC 6302: the lobes, expanding fast with a Hubble flow, the molecular torus, expanding slowly at $\sim$8 km s^{-1}, and the inner ionized torus. This raises the question whether these components date from separate mass-loss events, or have a common origin.

Peretto et al. (2007) derived the timing and duration of the mass-loss event which lead to the formation of the torus. This event lasted $\approx$4600 yr, began 7500 yr ago and finished $\approx$2900 yr ago. Fig. 11 indicates the duration of this mass-loss phase as a vertical bar. The present work estimates the age of the lobes to be $\approx$2240 yr. Thus, the lobes formed after the torus was ejected, and there appears to be a delay of $\sim$650 yr between the ejection of the torus and lobes. The inner torus has a reported age of 1200 yr, but this needs confirmation.

Differences in time between the ejection of a torus and of a jet are known from other objects. Huggins (2007), based on a sample of nine nebulae for which both times were available, found that there was a small delay of typically a few hundred years between torus and jets. For this time delay pattern he coined the term *jet lag*. The fact that this statistical effect is confirmed in this detailed study of the lobes and torus of NGC 6302 provides support for this mass-loss description.

Excluding the innermost torus, we find a mass-loss history for NGC 6302 consisting of a slow, dense, equatorial wind with mass-loss rates of $\dot{M} \sim 5 \times 10^{-4}$ M$_\odot$ yr^{-1}, lasting for roughly 5000 yr, followed by a brief interlude, before a short-lived event caused the formation of the fast, bipolar lobes.

Assuming a lobe mass of ~ 0.5 M$_\odot$ (Dinh-V-Trung et al. 2008), the mass-loss rate of the rapid lobe ejection would seem to be extreme. However, it is more likely that this event accelerated gas previously ejected.

Peretto et al. (2007) argue that the momentum of the torus is almost an order of magnitude larger than that in the stellar radiation field. The lobes, moving much faster, having a few times less mass but having formed at least 10 times faster, have a much higher ratio of momentum to that in the stellar radiation field over the time of the ejection. This suggests the late ejection was energy driven, as has been suggested for other bipolar post-AGB stars (Bujarrabal et al. 2001).

Bujarrabal et al. (2001) suggest as one possibility that the fast outflows are driven by conversion of gravitational energy of re-accreted material into bipolar jet momentum. This model can also be proposed for NGC 6302. Peretto et al. (2007) suggest that the torus ejection was aided by a binary companion. In this case, the later fast flows could be powered by an accretion disc around the same binary companion.

5 CONCLUSIONS

The comparison of two *HST F*658*N* images allowed for measurement of the PM vector for 200 4.1×4.1 arcsec^2 square tiles predominantly across the eastern lobe. The resultant velocity field is very regular and largely radial. We have shown that the Hubble flow relation extends into the innermost parts of the nebula. The age of 2250 yr of the nebula agrees with the one derived for north-western lobe by Meaburn et al. (2008). The inner parts of the nebula show evidence of additional acceleration which took place only in the recent history of the nebula. The additional velocity component is more clearly pronounced in the southern half of the lobe, than in the northern. We attribute this recent acceleration to overpressure after the onset of ionization.

The criss-cross mapping indicates that the PM velocity field points towards the central star reported by Szyszka et al. (2009). It also shows that the lobes and the torus have the same kinematic origin, close to the central star. The comparison of torus ejection time with lobe ejection time provides further evidence that these two events, although separated in time, are linked together.

The mass-loss history for NGC 6302 shows a phase of equatorial, slow mass loss at a high rate of $\dot{M} \sim 5 \times 5 \times 10^{-4}$ M$_\odot$ yr^{-1}, lasting about 5000 yr, and followed by an interlude of $\sim$650 yr before the fast lobes formed during a short-lived, energetic event. We suggest that the lobes may have formed through an accretion disc around a companion to the central star.

ACKNOWLEDGMENTS

We would like to thank W. Steffen for his assistance in preparing the criss-cross map. We also thank the anonymous referee whose careful reading of the manuscript leads to improvements of this paper. CS is grateful to the University of Manchester, School of Physics and Astronomy, for a bursary.

This research made use of MONTAGE, funded by the National Aeronautics and Space Administration's Earth Science Technology Office, Computation Technologies Project, under Cooperative Agreement Number NCC5-626 between NASA and the California Institute of Technology. MONTAGE is maintained by the NASA/IPAC Infrared Science Archive. Based on observations made with the NASA/ESA Hubble Space Telescope, and obtained from the Hubble Legacy Archive, which is a collaboration between the Space Telescope Science Institute (STScI/NASA), the Space Telescope European Coordinating Facility (ST-ECF/ESA) and the Canadian Astronomy Data Centre (CADC/NRC/CSA).

REFERENCES

Balick B., Frank A., 2002, ARA&A, 40, 439
Bujarrabal V., Castro-Carrizo A., Alcolea J., Sánchez Contreras C., 2001, A&A, 377, 868
Corradi R. L. M., 2004, in Meixner M., Kastner J. H., Balick B., Soker N., eds, ASP Conf. Ser. Vol. 313, Asymmetrical Planetary Nebulae III: Winds, Structure and the Thunderbird. Astron. Soc. Pac., San Francisco, p. 148
Dinh-V-Trung Bujarrabal V., Castro-Carrizo A., Lim J., Kwok S., 2008, ApJ, 673, 934
Evans D. S., 1959, MNRAS, 119, 150
Gesicki K., Acker A., Zijlstra A. A., 2003, A&A, 400, 957
Gomez Y., Rodriguez L. F., Moran J. M., Garay G., 1989, ApJ, 345, 862
Gomez Y., Rodriguez L. F., Moran J. M., 1993, ApJ, 416, 620
Guzmán L., Loinard L., Gómez Y., Morisset C., 2009, AJ, 138, 46
Habing H. J., 1996, A&AR, 7, 97
Hajian A. R., Terzian Y., Bignell C., 1993, AJ, 106, 1965
Huggins P. J., 2007, ApJ, 663, 342
Icke V., 2003, A&A, 405, L11
Jones D., Lloyd M., Mitchell D. L., Pollacco D. L., O'Brien T. J., Vaytet N. M. H., 2010, MNRAS, 401, 405
Lasker B. M. et al., 2008, AJ, 136, 735

Downloaded from https://academic.oup.com/mnras/article/416/1/715/1217193 by guest on 24 April 2024

Markwardt C. B., 2009, in Bohlender D. A., Durand D., Dowler P., eds, ASP Conf. Ser. Vol. 411, Non-linear Least-squares Fitting in IDL with MPFIT. Astron. Soc. Pac., San Francisco, p. 251
Masson C. R., 1986, ApJ, 302, L27
Matsuura M., Zijlstra A. A., Molster F. J., Waters L. B. F. M., Nomura H., Sahai R., Hoare M. G., 2005, MNRAS, 359, 383
Meaburn J., 1997, MNRAS, 292, L11
Meaburn J., Walsh J. R., 1980, MNRAS, 193, 631
Meaburn J., López J. A., Steffen W., Graham M. F., Holloway A. J., 2005, AJ, 130, 2303
Meaburn J., Lloyd M., Vaytet N. M. H., López J. A., 2008, MNRAS, 385, 269
Palen S., Balick B., Hajian A. R., Terzian Y., Bond H. E., Panagia N., 2002, AJ, 123, 2666
Peretto N., Fuller G., Zijlstra A., Patel N., 2007, A&A, 473, 207
Skrutskie M. F. et al., 2006, AJ, 131, 1163
Steffen W., Koning N., Wenger S., Morisset C., Magnor M., 2010, IEEE Trans. Visualization and Comput. Graphics, doi:10.1109/TVCG.2010.62
Steffen W., Koning N., 2011, AJ, 141, 76
Szyszka C., Walsh J. R., Zijlstra A. A., Tsamis Y. G., 2009, ApJ, 707, L32
Tsamis Y. G., Barlow M. J., Liu X., Danziger I. J., Storey P. J., 2003, MNRAS, 345, 186
Zijlstra A. A., Chapman J. M., te Lintel Hekkert P., Likkel L., Comeron F., Norris R. P., Molster F. J., Cohen R. J., 2001, MNRAS, 322, 280
Zijlstra A. A., van Hoof P. A. M., Perley R. A., 2008, ApJ, 681, 1296

This paper has been typeset from a TEX/LATEX file prepared by the author.

Downloaded from https://academic.oup.com/mnras/article/416/1/715/1217193 by guest on 24 April 2024